Image clustering for overtopping volume measurements

Manuscript submitted to Physics of Fluids for review and possible publication

IMAGE CLUSTERING FOR OVERTOPPING VOLUME MEASUREMENTS

Sara Mizar Formentin[1], Corrado Altomare[2], Andrea Marzeddu[2] and Barbara Zanuttigh[1].

(1) Department of Civil, Chemical, Environmental and Materials Engineering, Università di Bologna, Viale del Risorgimento 2, Bologna 40136, Italy.
saramizar.formentin2@unibo.it

(2) Maritime Engineering Laboratory, Universitat Politècnica de Catalunya - BarcelonaTech, Carrer de Jordi Girona 1-3, Campus Nord, Edifici D1, Barcelona 08034, Spain

Abstract

The representation of the wave overtopping is of unquestionable relevance for the assessment of the coastal and harbor safety and for the design of coastal defenses. The direct measurement of the wave overtopping volumes and discharges is a common practice in the laboratories, but it requires the installation of specific devices and instrumentation and may cause disturbance to the experiments. This contribution presents a procedure based on the image clustering to estimate the individual and the total overtopping volumes at coastal structures, while capturing the time-spatial evolution of the overtopping flow and avoiding any disturbance to the process itself. The procedure is validated against laboratory tests of focused waves on a sloping dike with a gentle and shallow foreshore and provided accurate and reliable estimations of the wave overtopping. The procedure automatically detects the individual overtopping volumes and its adaptability to different test conditions and structural configurations is proved. Requiring essentially a video camera to film the wave overtopping, the image clustering procedure can be applied also to prototype and field experiments, where the measurement of the wave overtopping may result complicated or unaffordable.

Keywords: videography; image clustering; wave overtopping; overtopping volumes; focused waves; non-intrusive monitoring.

1. Introduction

The evaluation of wave overtopping plays a pivotal role in assessing the efficacy and resilience of coastal structures with the primary objective of minimizing damage caused by seawater overflow from waves, safeguarding assets, infrastructure, and human lives. Owen (1980) initiated the groundwork for overtopping assessment, selecting average discharge as a design parameter, given the significant variation in individual overtopping volumes. Semi-empirical formulas, commonly employed for overtopping assessment under specific wave conditions and water levels (e.g. Altomare et al., 2016; EurOtop, 2018; Altomare et al., 2020a; Gallach-Sanchez et al., 2020; Yuhi et al., 2021; Lashley et al., 2021; van Gent et al, 2022), typically rely on simplified sections of coastal defenses. Despite machine learning techniques addressing some limitations in these formulas (Zanuttigh et al., 2016; den Bieman et al., 2021; Mares-Nasarre et al., 2024), they still necessitate homogeneous and extensive training databases. Notably, these approaches predominantly concentrate on evaluating mean overtopping discharge. However, Ingram et al. (2008) proposed that research should have prioritized understanding and quantifying post-overtopping effects.

There is a recent call for revising hazards associated with overtopping, based on mean discharges, and establishing new criteria rooted in individual overtopping flow properties (Sandoval and Bruce, 2018; Mares-Nasarre et al., 2019; Altomare et al., 2020b; Suzuki et al., 2020; Koosheh et al., 2024). A critical aspect lies in enhancing the comprehension of individual overtopping flows to provide guidance for the design of coastal structures (Hughes and Thornton 2016; Formentin and Zanuttigh, 2019; Formentin et al., 2019). In fact, it is crucial to consider the risks posed by specific overtopping events, such as sweeping pedestrians off their feet or requiring evacuation countermeasures, and take decisive measures to mitigate them. Therefore, accurately predicting and characterizing large overtopping events is crucial in certain situations.

Deterministic, physics-based approaches are available for estimating maximum overtopping events. Determining the maximum volume associated to overtopping events during a sea storm, V_{max}, relies on assumed probability distributions of volumes (van der Meer and Janssen, 1994; Zanuttigh et al., 2013; Nørgaard et al., 2014; Koosheh et al., 2022).

Gaining a comprehensive understanding of all processes involved in wave overtopping necessitates accurate measurements of the physical phenomenon. Numerical methods can simulate wave-structure interaction and analyze the wave-by-wave process, though with a significant effort for the preparation of the required data and the need for calibration and with some simplification and limitations. CFD solvers based on Volume-Of-Fluids (VOF) methods (e.g., OpenFOAM® with waves2Foam package, Jacobsen et al., 2012) generally well reproduce the wave overtopping (e.g., Patil, 2019; Chen et al., 2021), but often underestimate turbulence effects and time to time fail to reproduce wave aeration correctly (Chen et al., 2021). The inclusion of turbulence closure models or compressible solves to achieve a more realistic representation of the physical phenomena may affect the numerical stability and significantly aggravate the computational effort. Lagrangian methods, such as Smoothed Particle Hydrodynamics (SPH) (Violeau, 2012; Crespo et al., 2015; Domínguez et al., 2022) allow

overcoming part of the drawbacks associated to mesh-based schemes and are inherently capable to capture non-linearities. However, they still require further improvements to resolve the hydrodynamics of the individual flow properties, while keeping reasonable computational costs (Altomare et al., 2021).

In an effort to advance the understanding and characterization of overtopping volumes, this article pretends to contribute by employing non-intrusive monitoring techniques. These methods aim to offer novel perspectives on the hydrodynamics of wave overtopping, providing insights that may enhance our knowledge of the complex processes involved in these events. Their employment has been constantly increasing in recent years with the spread of video imagery techniques – such as laser scanner (Hofland et al., 2015; Oosterlo et al., 2021; Blenkinsopp et al., 2022), Particle Image Velocimetry (Stansby and Feng, 2004; Cao et al., 2021) and Bubble Image Velocimetry (Raby et al., 2020; Adibhusana et al., 2023), monitoring systems (Fairley et al., 2007; Chi et al., 2021) and high-speed cameras (Adibhusana et al., 2024) – gaining status as efficient and reliable methods alternative to physical measurements and numerical modelling, eventually becoming part of the state-of-the art techniques for the wave overtopping modelling.

In such a context, following the stream of machine-learning techniques for reconstructing quantitative data from video imagery (Stringari et al., 2019; Buscombe et al., 2020; Den Bieman et al., 2020; Stringari et al.,2021; Formentin et al., 2021; Formentin et al., 2023), this contribution presents an innovative methodology to estimate the individual and the total wave overtopping volumes at coastal structures based on the image clustering. The methodology was developed and applied to video-records of laboratory experiments of wave overtopping conducted against sloping dikes in the CIEMito flume Laboratory of Universitat Politècnica de Catalunya – BarcelonaTech (LIM/UPC). Despite existing studies have been already employed image-based methods to study the wave overtopping (e.g., Raby et al., 2020; Cao et al., 2021; Blenkinsopp et al., 2022; Adibhusana et al., 2023; Adibhusana et al., 2024), to the authors' best knowledge the present study represents the first contribution developed to directly estimate the wave overtopping volumes.

The paper is structured into distinct sections, each addressing specific aspects of the research. Section 2 outlines the experimental set-up. In section 3, the image clustering technique is detailed. The algorithm to calculate the overtopping volumes from the detected clusters is explained in Section 4, while uncertainties of the methodology are discussed in Section 5. Validation and application cases are presented in Section 6. Finally, Section 7 delves into a discussion of the findings and draws conclusions from the study.

2. Experimental model

2.1. Model setup

The experimental campaign was carried out in the small-scale wave & current flume called CIEMito at the Maritime Engineering Laboratory of Universitat Politècnica de Catalunya –

BarcelonaTech (LIM/UPC). The CIEMito flume, measuring 18 meters in length and 0.38 meters in width, uses a piston-type wavemaker for wave generation in a scaled-down 1:50 model. The model is made of plywood and includes a dike at the end of a sloping foreshore that is designed to induce wave breaking before reaching the structure's toe. Different foreshore slopes and dike geometries were considered, including a vertical wall and sloping dikes. For the purpose of developing the methodology, we analyzed wave overtopping on dike slopes with a ratio of 1V:2H and a foreshore with length of about 5 meters. The foreshore was composed of 5 modular plywood elements, each 1 meter long. The last element had a slope of 1V:22.6H. The slope of each element is indicated in the figure. A scheme of the experimental setup is depicted in Figure 1. The height of the dike was kept constant at 0.04 m. Different dike geometries and foreshore slope have been employed for further application of the method: they are described in Section 6.

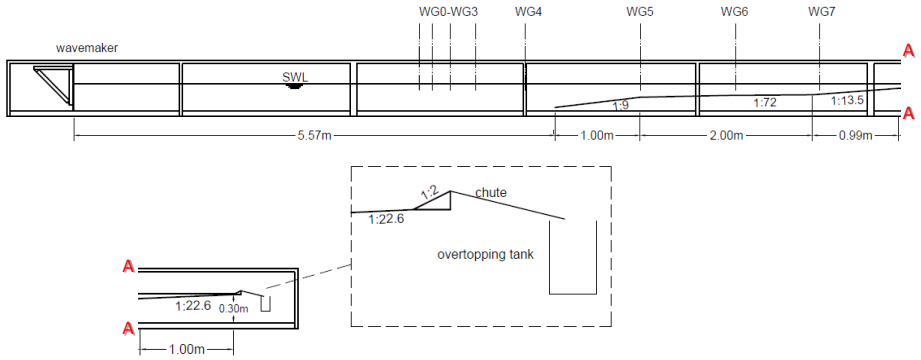

Figure 1. Experimental model setup in the CIEMito flume

Resistive wave gauges along the flume measured water surface elevation, while an overtopping tank, equipped with an ultrasonic proximity sensor, quantified the volume of overtopping. Location of the wave gauges is indicated in Table 1. An IDS UI-31800CP-M-GL video camera recorded images with a resolution of 5.1 megapixels. A compromise between sampling frequency and image resolution was achieved by shooting at 106 fps, with captured images at a resolution of 1900x1080 pixels. By a careful setting up the camera, the depth of field (DOF) was limited. The DOF is defined as the distance within which objects captured by the camera are well focused and appear to be sharp. Assuming that a lens focuses on a point at a distance L from the forward nodal point of the lens (which is sufficiently close to the distance between the lens front and the point), the DOF can be calculated using the formulae defined in Ray (2002), depending on the focal length of the camera focal lens and the f-number of the camera aperture. The camera was perpendicular to the glass walls at one side of the wave flume facing the measuring window exactly where the dike was placed. The lens was therefore calibrated to focus on a point at a distance from the centre of focal plane equal to 0.60 m, with a *f-number*=2.8 and a focal length *f*=55 mm. The calculated DOF resulted equal to 0.02m. The focal plane was positioned at a

distance of approximately 10 cm from the glass wall of the flume, in order to minimize the potential for distortion due to the glass itself and the mounting structures on the foreshore. The illumination system included a high-power LED lamp constructed in-house using five lines of high-power LED lamps on a mobile frame atop the flume walls. The Norpix StreamPix 7 high-speed digital recording software was used for recording the video images. The camera filming frame was set up to capture the whole overtopping flow behind the dike. The video-records of the wave impacts were elaborated with the image clustering technique developed by Formentin et al. (2021).

Table 1. Resistive wave gauge location

Wave gauge	WG0	WG1	WG2	WG3	WG4	WG5	WG6	WG7
Distance from the wave maker (m)	4	4.15	4.36	4.65	5.23	6.56	7.67	8.64

2.2. Hydrodynamic conditions: focused wave groups

To ensure accurate structural design of coastal defenses, Hughes and Thornton (2016) and Whittaker et al. (2018) emphasized the necessity of considering individual wave properties. Incorporating short-duration focused wave groups into the design approach can complement long-duration irregular wave tests. This can result in advantages such as increased repeatability, assessment of model and scale effects, potential for enhanced measurement, and improved model resolution for large wave interaction. Additionally, the use of focused wave groups eliminates the need for wave absorption. Whittaker et al. (2016) validated the use of focused wave groups for WSI (Wave-Structure Interaction) problems. They suggested that a single incident wave group could replicate extreme coastal responses within a specific sea state. For such reasons, in this study, focused wave groups were utilized instead of random sea states.

The time series for each focused wave group was generated using the NewWave theory, as detailed in Whittaker et al. (2017). This theory outlines the most probable shape of a large wave in a given sea state. While NewWave originally describes the generation and propagation of a compact wave train on a horizontal bottom, it is adapted here for waves shoaling and breaking near a structural location. The focus location is employed to control the dispersion of the wave group as it shoals and breaks during propagation. Whittaker et al. (2016) demonstrated that the NewWave theory remains valid in relatively shallow waters (kh<0.5), indicating that linear frequency dispersion continues to be the dominant mechanism despite the increasing importance of nonlinear effects due to changes in bathymetry. Theoretically, the focus wave group energy reaches the structure in a compact, maximized form if the focus location is close enough to the structure. A NewWave-type focused wave group comprising N infinitesimal wave components is given by:

$$\eta(x,t)=\frac{A}{\sigma^2}\sum_{i=1}^{N} S_{\eta\eta}(\omega_i)\cos(k_i(x-x_f)-\omega_i(t-t_f)+\phi)\,\Delta\omega \quad (1)$$

where $S_{\eta\eta}$ is the power spectral density, ω is the angular frequency, t is time, σ is the standard deviation of the sea state (with an associated variance $\sigma^2=\sum S_{\eta\eta}(\omega_i)\Delta\omega$ in this discretized form) and k_i is the wavenumber of the i-th wave component with angular frequency ω_i and related to it by the familiar linear dispersion relation $\omega^2=gk*tanh(kh)$ (where g is the acceleration due to gravity and h is the water depth), and x is the horizontal distance. All wave components come into phase at the focus location x_f and focus time t_f to form a large wave with a linear focus amplitude equal to A. A full range of focusing behaviours can be allowed by introducing the the phase angle ϕ of the group at focus (e.g. crest, trough, otherwise), while the energy concentration within the group is independent of the value of ϕ. However, the wave shape can affect its breaking patterns and therefore the impacts exerted on the structure.

For the sake of the methodology development, one focused wave group conditions out of the experimental campaign carried out in the CIEMito flume has been selected. The experiment consisted of focused waves generated starting from the following spectral wave characteristics: H_{m0}=0.08 m, T_p=1.6 s, for an initial water depth of 0.31 m. Water depth at the dike toe resulted equal to 1 cm. Focus location was equal to 9.58 m, measured from the wavemaker at rest, while a 90° focus phase was employed. Such experiments will be referenced as "Test_α2m22.6" hereinafter, where m is the foreshore slope and α is the dike slope, both expressed by the cotangent of the slope angle with the horizontal (i.e. α2=1V:2H, m22.6=1V:22.6H).

Scale effects have been examined, due to the relatively small scale here employed. To determine the limiting criteria for flow-structure interaction, Heller (2011) recommended investigating scales that balance model size and scale effects. According to EurOtop (2018), large-scale tests for vertical structures validate the scalability of formulas derived from small-scale studies (Pearson et al., 2002). However, despite these assertions, further examination is required to fully dismiss scale effects. The analysis focuses on viscous forces and surface tension, in accordance with EurOtop (2018). Reynolds and Weber numbers for wave overtopping (*Req* and *Weq*) are calculated and compared to the critical limits (*Req* > 10^3 and *Weq* > 10), as defined by Schüttrumpf and Oumeraci (2005). The calculation of *Req* and *Weq* involves evaluating the run-up of focused wave groups, overtopping flow velocity, and depth. To aid in the calculation of *Req*, wave run-up estimation, as described by Yuhi et al. (2021), is used. For the calculation of *Weq*, the overtopping flow velocity and depth were derived from EurOtop (2018). The calculated *Req* and *Weq* for the case used to develop and validate the presented methodology were equal to 9600 and 280, respectively, which are larger than the critical thresholds. According to Heller (2011), this indicates the impact of scale effects is very small or almost negligible to the sake of wave overtopping estimation. This check was also carried out for the further cases presented in Section 6, which also showed the negligible relevance of scale effects. The impact of scale effects on air entrainment and bubble distribution and fragmentation, although relevant, is beyond the scope of this study. For further insight, please refer to Miller (1972), Deane and Stokes (2002) and Stagonas et al. (2011).

3. Image clustering

3.1. Description of the procedure

The data were analyzed using a new image-processing method, which was developed by building on the existing methodology used by Formentin et al. (2021) to reconstruct free-surface profiles from video recordings of wave overtopping tests. Formentin et al. (2021) had introduced specific procedures for analyzing overtopping and overflow processes above coastal dike crests. The task involved evaluating flow depths and celerity, as well as estimating the amount of air bubbles trapped in the flow during wave breaking. Formentin and Zanuttigh (2023) have recently introduced revised procedures for estimating wave run-up at crown walls.

The methodology used involves applying the image-clustering technique to automatically recognize and group different classes of objects in the images, such as 'water', 'air', 'solid structure', etc. This is supported by pre- and post-clustering techniques to optimize image detection, as well as procedures that manipulate the outputs of the image clustering to obtain quantitative information of practical interest. In the following, the main steps and the workflow of the existing procedure are briefly exposed:

i) Pre-clustering: before applying the clustering, the images need to be "fit" – in terms of color, contrast, brightness, noise – to optimize the automatic detection of the different objects. The pre-clustering procedures may change from application to application, depending on the type and number of patterns to be identified; therefore, such operations can be hardly standardized. Generally, the pre-clustering techniques involve: image subtraction to level uneven sections of an image, such as shadows, reflexes or blurs, and to remove unwanted fixed elements potentially present in all the frames; conversion into grayscale; noise add, if large portions of the images may result too uniform for the pattern recognition; contrast enhancement and light adjustment. Figure 2(b)

ii) Training of the cluster model: such step consists in the creation of the model which detects and distinguish the different "objects" composing a frame and fits them into separate clusters. Such model is therefore meant to be used as a reference for all the frames of a video-record. A cluster model map is a sort of hyper-figure, where each of its pixels is associated to a label identifying the belonging cluster. Figure 2 shows an example of a frame selected to train a cluster model (panel a) and the corresponding cluster model map (panel c) obtained, where the different colors identify the different clusters of objects detected. The training step involves the following key aspects: definition of the number of clusters, selection of the training algorithm, and individuation of the frame itself to be clustered and used as model. The best configuration of such training features can be defined only *a-posteriori*, i.e. after a trial-and-error process of attempts searching for the model map that best captures the "objects" in the images according to the research purpose. It is important to remind that the association cluster-"real object" relies on the human interpretation of the clusters in the model map: in the example of Figure 2c, where four clusters are identified, cluster 2 (green) groups the "dark" objects, which are either the dike structure, the "steady"

part of the flow beneath the free-surface, and the black background; clusters 3 and 4 (blue and purple, respectively) both refer to the turbulent part of the flow, the free-surface and the entrapped bubbles, capturing different shades of light; cluster 1 (yellow) eventually represents the blurry areas surrounding the water flow and the structure in foreground, corresponding to background elements partially visible because of perspective effects in the picture. The details of the selected features to train the cluster model for the present research study are given in Sub-Section 3.2.

iii) Clustering: once trained the cluster model, all the images to be analyzed can be processed with the pre-clustering techniques and then clustered. With the clustering, each image is converted into a cluster model map similar to the one in Figure 2c, where each pixel is labelled according to the belonging group.

iv) Post-clustering and output manipulation. This step includes all the procedures to be applied to the clustered images to extract the quantitative information desired. Therefore, the number and the type of the post-clustering procedures, strictly depend on the process to be modelled and on the expected results. The post clustering procedures need to be adapted and redesigned each time a new phenomenon is studied. In Formentin et al. (2021), post-clustering procedures were built to reconstruct the free-surface profile and elaborate the edges of the "water" objects, whereas Formentin and Zanuttigh (2023) developed post-clustering procedures to calculate the wave run-up at walls. In this paper the post clustering technique has been selected and adapted for the estimation of the overtopping volumes and are described in Sub-section 3.3. The procedure for the estimation of the overtopping volumes itself represents the core of the present study and is illustrated in Section 4.

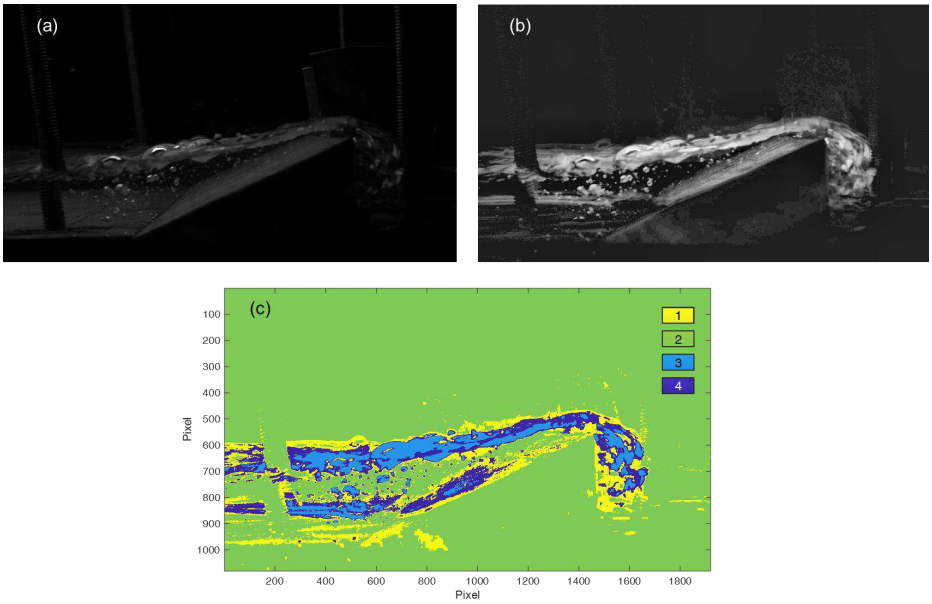

Figure 2. a) image of an example frame selected for training the cluster model as taken with the camera; b) result of the image transformation after applying the pre-clustering techniques; c) cluster model map of the image in false colors.

3.2. Selected features for the pre-clustering and clustering steps

The pre-clustering techniques and the training of the cluster model were adapted to fit the scope of the present research. The adaptation was based on a trial-and-error procedure which involved: i) the definition of the camera framing window; ii) the setup of the camera's resolution, focus, focal length and aperture time (not all of them can be set independently and they have been adjusted to achieve the best quality image); iii) the setup of the laboratory facility to individuate the best conditions of lighting, and background; iv) the individuation of the set of light, contrast, and noise filters to optimize the image clustering; v) the individuation of the most suitable set of features to perform the cluster training. Details of the experimental setup (steps i) to iii)) can be found in Section 2.

For step iv), the following set of filters was applied to the images before applying the image clustering:

- Image subtraction: one still image taken before the start of the experiments was selected in order to subtract from all the frames of the video-record some fixed elements present in the camera field of view, such as the threaded screws in the middle of the channel to hang the bottom, and blurs and shadows in the background.

- Image brightness enhancement: the brightness of the images was enhanced by increasing the value of each pixel by 20 to improve pattern recognition during the image clustering.
- Contrast enhancement: the contrast of each image was enhanced using a contrast-limited adaptive histogram equalization; a uniform histogram with a contrast enhancement limit = 0.05 was established. Similar to brightness, contrast enhancement improves pattern recognition by sharpening the edges of the elements that make up an image.

The image transformation obtained with such filters is portrayed in Figure 2, where panel (a) shows the original frame as taken from the camera, and panel (b) shows the same frame as resulting after the application of the filters.

Cluster training was performed with the open source toolbox "PRTools" (Pattern recognition tools, http://prtools.tudelft.nl/?from=www.website80.com, Duin and Pekalska, 2015), selecting the Expectation–Maximisation (EM) algorithm (Dempster et al., 1977) and the 'crisp' labelling type of the patterns, which applies a boosted version (generalized *k-means* algorithm) of the traditional EM algorithm. The fundamental issue in a partitioning clustering, such as *k-means* clustering, is the definition of the number of clusters, because it determines the number of "interesting patterns" to be discovered in an image. In the present application, the number of clusters was set equal to 4: it was indeed found that a smaller number was not sufficient to properly capture the profile of the water flow, because in some darker parts of the image the water pattern was mixed up with the background color; on the contrary, a higher number of clusters led to the fragmentation of the water flow into multiple patterns. The result of the cluster training applied is shown in Figure 2c, where the overtopping flow – objective of the present application – can be identified with the clusters 3 and 4 (blue and purple).

3.3. Post-clustering optimization

After performing the image clustering, all the frames that make up the video record of an experiment are transformed into cluster maps such as the example in Figure 2c. Such maps can be considered as "hyper-figures" – or datasets – since each of their pixels is labelled according to the belonging cluster. The post-clustering represents the step of the methodology where the information embedded in the clustered hyper-figures is extracted and elaborated for further applications – viz the wave overtopping calculation.

Similar to the pre-clustering and clustering steps, the post-clustering techniques were also set up based on a trial-and-error process. In this case, the following procedures were applied to each frame.

- Image segmentation: all the areas of the image composed by pixels belonging to the cluster associated to the overtopping flow were selected and the corresponding edge extracted. Segmentation was performed through the 'Canny' algorithm (Canny, 1986), which finds the edges by looking for local maxima of the gradient of the image. The Canny edge function calculates the gradient using the derivative of a Gaussian filter using two thresholds to detect strong and weak edges. By using two thresholds, the Canny method is less likely

than other methods to be fooled by noise, and more likely to detect true weak edges. Figure 3a shows the contour (blue) of the objects enclosed in the cluster associated to the overtopping flow.

- Removal of small connected components: the contour of the overtopping flow areas returned by the image segmentation includes several fragmented parts or elements that represent only scatter or noise. In Figure 3a, many small fragmented elements are present, for example, in the red-circle area. The removal of such parts was done through the application of a morphological filter based on the size of the areas of the "connected components". Precisely, all the connected components of the "overtopping flow" characterized by areas counting less than 100 pixels were removed by the application of such a filter. The result of the morphological filter applied to Figure 3a is shown in Figure 3b.

With respect to the previous works by Formentin et al. (2021) and Formentin and Zanuttigh (2023), it was not necessary to apply any further post-clustering technique, mainly thanks to the significantly higher quality characterizing the original images.

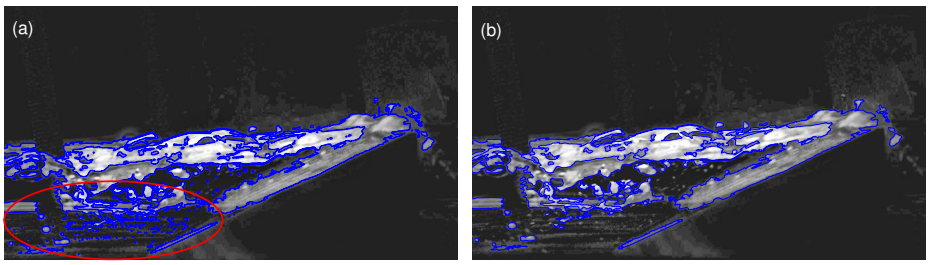

Figure 3. a) Contour (blue) of the cluster "overtopping flow" detected in an example frame as a result of the image segmentation, showing many fragmented small elements as in the red circle; b) Refinement of the contour after application of the filter to remove the small connected components.

4. Wave overtopping volumes calculation

The core and newest part of the methodology is represented by the procedure for calculating the waves overtopping volumes, which was specifically developed for the present study. This procedure is based on the calculation of the areas of the overtopping flow over the dike crest, which are used as a direct estimator of the individual, specific overtopping volumes ($m^3/(m \cdot frame)$). The procedure is meant to be applied to each overtopping event, which may last several frames (namely, N frames), and is able to automatically catch the beginning and the end of each overtopping event. Triggering is based on temporal analysis of successive frames clustered to trigger the minimum area.

4.1. Description of the procedure

The procedure of calculation of the individual overtopping volumes is structured as follows.

i) Mask application: a mask is applied to each clustered frame to isolate the overtopping flow and remove all other elements of water. The mask works by imposing all the values of the pixels seaward to the dike crest equal to zero. Note that the mask has been thoroughly applied to all the frames of all the tests presented in such contribution, but it was decided to omit it in Figures Figure 4c, Figure 4d, Figure 7, 9 and Figure 10 to avoid the inclusion of images which otherwise would appear almost completely black.

ii) Triggering: the procedure starts when a 'non-negligible' amount of "overtopping flow" is detected to rise above the crest of the dike in a certain frame, which becomes the "$frame_0$". The position, shape and the extension (pixels) of the overtopping elements of 'water' are noted. The extension of the area of "overtopping flow" is the individual overtopping volume associated to $frame_0$, and it is called "$volume_0$" (V_0). Right now, such area is in pixels, and will be converted into $m^3/(m \cdot frame)$ later.

iii) Image subtraction: then, the procedure moves on to the couple of frames immediately consequent to $frame_0$, namely "$frame_1$" and "$frame_2$". Once the areas of the "overtopping flow" are individuated in each frame, the pixel-by-pixel operation of the image subtraction "$frame_2 - frame_1$" is applied. Figure 4a and Figure 4b show the refined contours of the "overtopping flow" patterns (blue) of two example consecutive frames, that can be assumed as "$frame_1$" and "$frame_2$", respectively. Figure 4c highlights in false colors the result of the difference between the two areas of "overtopping flow" associated to $frame_1$ and $frame_2$. It is important to remark that the image subtraction $frame_2 - frame_1$ is not calculated between the measures of the areas (scalar operation), but among the matrix of pixels composing the areas of wave overtopping (matrix operation). Therefore, the image subtraction may give positive, negative or zero-pixel values, depending on the extent and the shape of the areas of "overtopping flow" present in the two consecutive frames. The value of the j-th pixel comprising the image resulting from $frame_2 - frame_1$ will be positive if the corresponding j-th pixel of $frame_2$ is labelled as "overtopping flow" but it is not in $frame_1$; it will be negative if the j-th pixel of $frame_1$ is labelled as "overtopping flow" but it is not in $frame_2$; it will be zero if the j-th pixel of both $frame_1$ and $frame_2$ are labelled as "overtopping flow". The three possible results of the subtraction are shaded in Figure 4c in magenta (positive), green (negative), and white (zero), respectively.

iv) Removal of negative areas: from a physical point of view, the difference between the areas of the overtopping flow resulting from two consecutive frames represents the instantaneous variation of the wave overtopping volume ΔV_1. The zero-pixel values (white) represent the areas of superposition of the overtopping flow between the two frames; the positive values (magenta) represent the areas of increment of wave overtopping, whereas the negative values (green) represent the areas of decrease of wave overtopping. For this reason, the instantaneous increment of wave overtopping volume ΔV_1 occurring between $frame_1$ and $frame_2$ is calculated as follows and calculated for positive areas only:

$$\Delta V_1 = \sum_{j=1}^{P} pixel_{j,frame_2} - pixel_{j,frame_1}, \text{ if } (pixel_{j,frame_2} - pixel_{j,frame_1}) > 0 \quad (2),$$

where P is the number of pixels composing the frames. The difference ΔV_1 is saved as "volume$_1$" and it is still measured in pixels. Figure 4d shows the sole positive areas of "water" resulting from frame$_2$ – frame$_1$, i.e. ΔV_1. The barycenter (or centroid) of ΔV_1 is reported in Figure 4d (red star) to observe that image subtraction "keeps memory" of the shape of the overtopping flow and its evolution in time and space. The information on the position of the centroid is important for the automatization of the procedure, as it will be illustrated in Sub-Section 4.2.

v) The image subtraction is then iteratively applied to all the subsequent frames, based on the following algorithm:

$$\Delta V_i = frame_{i+1} - frame_i, \text{ for } i = 1,\ldots,N-1 \quad (3),$$

where N is the last frame where wave overtopping is detected. Details on the procedure to automatically individualize the "N-th" frame and contextually stop the algorithm are given in Subsection 4.2.

vi) All the volumes from "$volume_0$" to "$volume_N$" are summed up and the total volume V associated to the single overtopping event is calculated:

$$V = V_0 + \sum_{i=1}^{N-1} \Delta V_i \quad (4).$$

vii) The measure of the total volume V is finally converted from pixels to m^3/(m·frame) by means of the conversion law reconstructed from the camera calibration process. The conversion ratio R is calculated by dividing the real, known length of the side of the squares in the checkerboard (20 mm) used to calibrate the camera by the length of the same side in pixels as resulting from the picture of the checkerboard itself. Then each individual volume V_0 or ΔV_i and the total volume V are multiplied by R^2, to have both the individual and the cumulative overtopping volumes. The propagation of the calibration error resulting from the conversion from a linear to a surface element can be calculated by doubling the initial linear error (see Section 5).

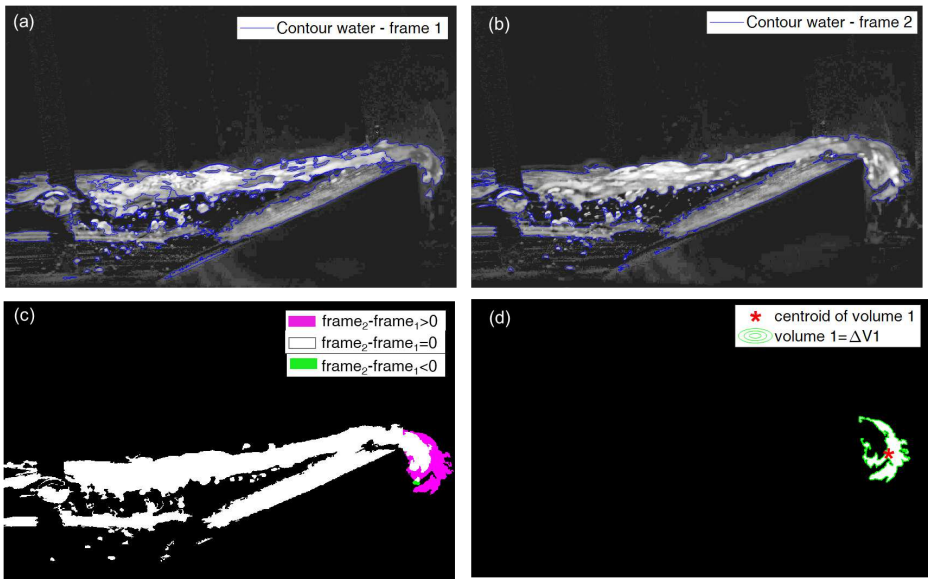

Figure 4. a-b) Refined contours (blue) of the "overtopping flow" cluster detected in two consecutive frames of wave overtake (that is, "$frame_1$" and "$frame_2$"); c) Result of the subtraction of "$frame_1$" from "$frame_2$", in false colors; d) area resulting from the image subtraction "$frame_2$ – $frame_1$", corresponding to "$volume_1$" or ΔV_1 (contoured by the green line) and corresponding centroid (red star).

4.2. Automatization of the procedure for multiple overtopping events calculation

The procedure for the calculation of the overtopping volumes includes a module to automatically identify the beginning and the ending of each individual overtopping event in a record containing multiple overtopping events. Such automatization may be redundant in case of focused waves, but it becomes essential to extend the procedure to the analysis of regular or irregular wave attacks, in order to individuate and separate consecutive overtopping events. The details of the automatization module are described hereinafter, with reference to Test_α2m22.6, as example application of the module itself. The 16 consecutive frames composing the first overtopping event of Test_α2m22.6 are shown in Figure 5, where the contours of the "overtopping flow" cluster are marked in blue.

4.2.1. Overtopping beginning

Without eye-analyzing the video-records of the experiments, it is not straightforward to establish whether a single or few pixels of "overtopping flow" present over the dike crest in a clustered frame do actually represent the beginning of an overtopping event and therefore trigger the

procedure. A small area of "overtopping flow" may correspond indeed to a drop, a spray, or even to noise "survived" to the post-clustering techniques. In the example of Figure 5a ($frame_1$), the flow is running up the ramp, but it has not yet reached the top of the dike. However, some drops of water (circled in red) are visible in the bottom right corner: such drops should not trigger the wave overtopping calculation. Instead, the procedure should start with $frame_2$ (Figure 5b), where the front tongue of the flow overtops the dike top and evolves into a larger area in the following $frame_3$ of Figure 5c.

To avoid the definition of a minimum threshold value of the overtopping area to start the procedure – which may vary with the test conditions, could be considered arbitrary or subjective and may lead to the underestimation of the total overtopping volume – a procedure of prescreening-analysis of the frames was developed. Such prescreening considers groups of three consecutive frames at once and evaluates, for each group, the presence of "overtopping flow" beyond the dike crest in each frame and compare the time-spatial evolution of its size and shape throughout the frames. Specifically, frames where the areas of "overtopping flow" which do not evolve across the following frames by either increasing their size or by moving forward, i.e. from seaward to landward, in the case of the present experiments, are skipped. To this end, the coordinates (abscissa x and ordinate z) of the centroid of the "overtopping flow" are evaluated over the three frames: a forward movement corresponds to an increase of the centroid abscissas (x-values), while a downward movement corresponds to an increase of the centroid ordinates (z-values). Note that the z-values increase downward in the intrinsic system of coordinates of the frames. The screening procedure progresses frame by frame until the centroid of an amount of "overtopping flow" appearing over the dike crest increases its x- and z-values for at least three consecutive frames. At this point, the overtopping volume calculation procedure is triggered, and the first of such three consecutive frames becomes the "$frame_0$" of the procedure. In the example of Figure 5 the "$frame_0$" of the procedure corresponds to $frame_2$ (Figure 5b): the centroid of the overtopping flow (red stars) moves indeed monotonically forward and downward from $frame_2$ to $frame_5$ at least. To appreciate the evolution of the position of the centroids over time, the position of the centroid of $frame_2$ is reported as a yellow cross in all the frames of Figure 5 for reference.

As a further reference, Figure 6b and Figure 6c show the time variation of the x- and z-coordinates of the centroids of the overtopping flow for overtopping event of Test_α2m22.6 portrayed in the frames of Figure 5.

476

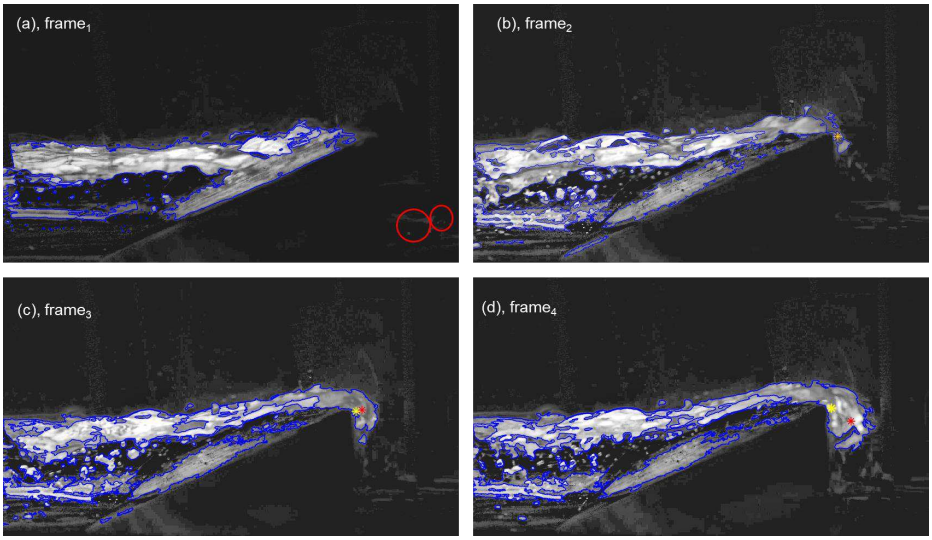

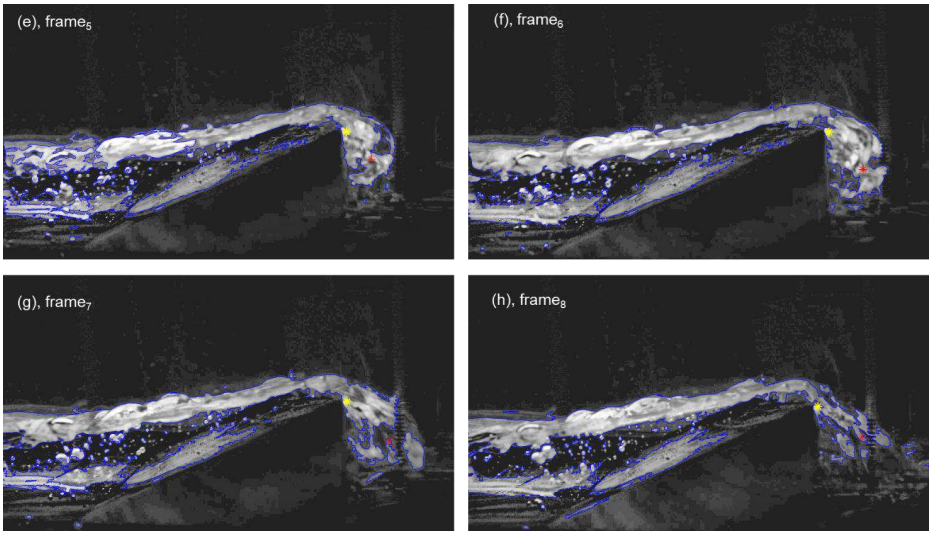

477

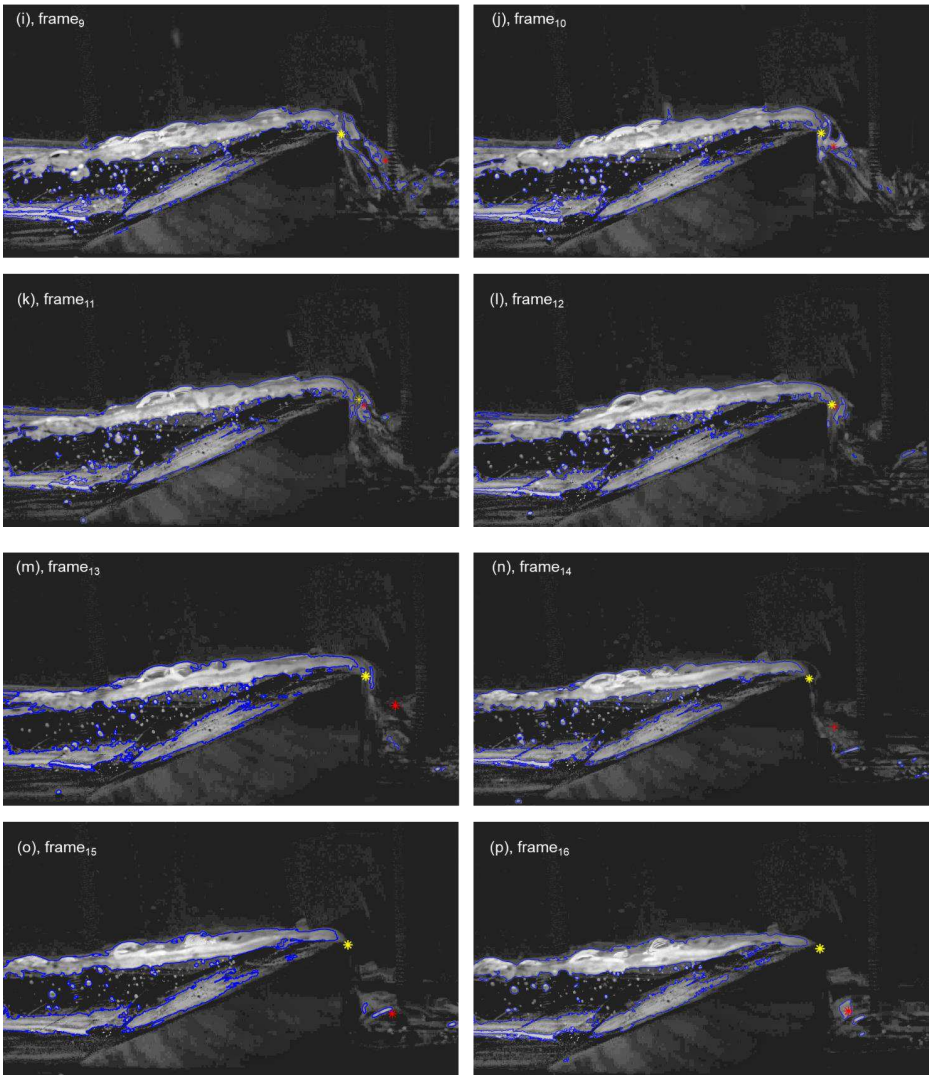

Figure 5. Refined contours (blue) of the cluster "overtopping flow" detected in 16 consecutive frames showing the beginning of an overtopping event. The procedure of calculation of overtopping volumes is made starting with *frame*$_2$ (panel b). The "drops" of "overtopping flow" in the red circles of *frame*$_1$ (a) do no trigger the procedure. In all the frames, the centroid of the current "overtopping flow" is reported (red star) in comparison to the centroid of *frame*$_2$ (yellow star).

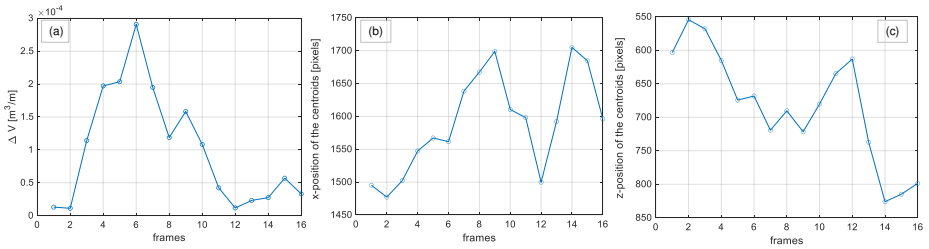

Figure 6. Time evolution of instantaneous increment of wave overtopping volumes ΔV (a), of the x-position of the centroids (b) and of the z-position of the centroids (c). The x- and z-positions are expressed in pixels. The origin of the coordinate system in the left-top corner of the frames, and the x- and z- coordinates increase towards right and downwards, respectively.

4.2.2. Overtopping ending

In Eq. (3), the sum of the ΔV-values is made stopping at the 'N-th' frame, which is defined as 'the last frame of wave overtopping". Similar to the activation of the procedure (Sub-section 4.2.1), the identification of the 'N-th' frame to stop the procedure is not straightforward. In general, such a 'N-th' frame cannot made be coinciding with the frame where no more pixels of "overtopping flow" are observed beyond the dike top, because in case of consecutive close-range overtopping events, a new event may begin when the previous one has not completely ended. Furthermore, some drops of water may have completely overtopped the dike top and yet still be present in the frames while propagating downward and forward, following a parabolic-like path before disappearing. This latter case can be appreciated in *frame*$_{13}$ to *frame*$_{16}$ of Figure 5, and it is remarked in Figure 7, which shows in false colors the ΔV-values obtained from the image subtraction of *frame*$_{11}$–*frame*$_{10}$, *frame*$_{12}$–*frame*$_{11}$, *frame*$_{13}$–*frame*$_{12}$ and *frame*$_{14}$–*frame*$_{13}$ of Test_α2m22.6. In this Figure, the last positive ΔV-value is ΔV_{11} of panel b, where the last magenta-shaded area is visible right beyond the dike crest. Figure 7c does not show any noticeable magenta area, whereas magenta fragments of overtopping flow are visible far from the dike top in Figure 7d and do not evidently correspond to new, positive contribution of overtopping.

Therefore, the individuation of the 'N-th' frame to stop the procedure must be related to the analysis of the evolution of the ΔV-values in time and space. The spatial evolution of ΔV over the overtopping event is tracked through the x- and z-coordinates of the centroids of the overtopping flow (Figure 6b and Figure 6c). The time evolution of ΔV for the example Test_α2m22.6 is shown in Figure 6a: this function describes a wave shape, characterized by a rise phase from frame$_2$ to frame$_6$, a maximum value and a decay phase, from frame$_6$ to frame$_{12}$. In correspondence of frame$_{12}$, the ΔV-function reaches a minimum: the eye-analysis of the frames of Figure 5 confirms that the entity of the overtopping flow increases between frame$_2$ and frame$_6$, it starts decreasing after frame$_6$ and eventually stops at frame$_{12}$. The trend-inversion

observed at $frame_6$ in Figure 5 and Figure 6a cannot be caught in Figure 6bc and Figure 6c, where the centroid continues moving landward and downward until $frame_9$. After this frame, however, the overtopping flow begins to retire and the centroid moves backward and upward until $frame_{12}$. At $frame_{12}$, the retire phase abruptly interrupts in both Figure 6b and Figure 6c, corresponding to the complete ending of the overtopping event. In conclusion, all the Figure 7and 7 indicate that the overtopping event ends at $frame_{12}$, determining ΔV_{12} as the last volume contribution. This analysis is converted into an algorithm that calculates the derivative of: i) the function ΔV for each frame, expecting positive, null, and negative values in sequence (corresponding to the phase of rise, peak, and decay of ΔV over time); ii) the x-coordinates of the centroid, expecting positive and negative values in sequence; iii) the z-coordinates of the centroid, expecting negative and positive values in sequence. When the expected values in the sequences are violated for more than two values consecutively and for all the derivates contemporarily, a trend inversion is supposed to happen and the procedure automatically aborts the calculation of the overtopping volumes. Then, the procedure starts to seek for a new overtopping event.

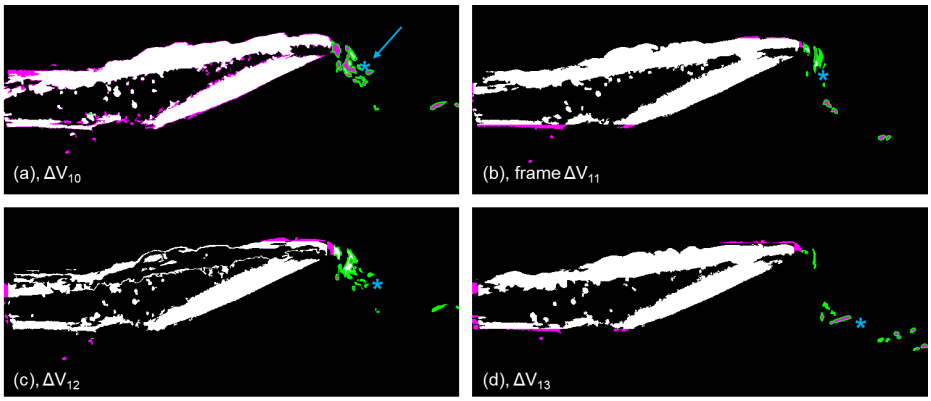

Figure 7. Result of the subtraction of 4 consecutive frames showing the ending of an overtopping event in false colors (positive, negative and zero increments of wave overtopping in magenta, green and white colors, respectively). The blue stars represent the centroids of the ΔV-values.

5. Uncertainty assessment

The uncertainty associated to the whole methodology for the computation of the wave overtopping volumes based on image clustering is determined by several contributions, some quantifiable and some not. The first contribution is determined by the conversion from pixels to meters, and depends on the accuracy of the camera calibration process. The conversion error

can be calculated by comparing the measurement of a known element in the picture in pixels with its corresponding real measurement in m. Such conversion error was estimated to be on average 2.1% for linear elements, and propagates as follows, for the conversion of surface areas: 2*2.1% = 4.2%. Another aspect relies on the correct selection of the cluster to represent the overtopping flow: in the example frame of Figure 2c, it is not evident whether the cluster that better represents the overtopping flow is the blue one (cluster 3) or the purple one (cluster 4) or the ensemble of the two clusters. In the end, cluster 3 was individuated, because after an eye-analysis of different cluster model maps obtained from different frames subjected to cluster training, it was understood that cluster 4 was associated to background unfocused elements, similarly to cluster 1. Such selection is even less straightforward in case of spurious blurs present in the frame, or when large numbers of clusters need to be imposed in the training step. Numerous clusters may be necessary in case of bad or uncontrolled light conditions, or of very "complicated" images characterized by several shades of colors or elements, typical of field experiments. All these conditions will determine the decomposition of the real "water element" into different clusters, making the selection of the "correct" cluster complicated. However, this phenomenon was ignored in the present study because the individuation of cluster 3 was pretty quick and its utilization optimized the computation of the overtopping flow. Actually, the lighting was specifically set up to optimize the rendering of the overtopping flow beyond the dike crest, disregarding the other parts of the picture.

Besides, there is the uncertainty strictly associated to the procedure of overtopping volumes calculation. Such uncertainty can be determined and will be illustrated and discussed in the Sub-sections 5.1 to 5.3. Finally, the uncertainty associated to the variability of the experimental measurement is addressed in Section 5.5.

5.1. Wave escape

It is possible that the procedure misses to capture part of the overtopping volumes if the combination of flow celerity, framing window size and sample frequency allows that a part of the overtopping flow "escapes" from the framing window in between the two frames. Such issue, may be avoided by setting the camera framing window and sampling frequency adequately to limit the phenomenon. Since the flow celerity (c) depends on the height of the overtopping flow (h) in the proportion $c \propto \sqrt{gh}$, being g the acceleration of gravity. In order to reduce the wave escaping it is recommended to set the dimension of the framing window *"s"* and the camera sampling frequency "*f*" such as that the product "$s \cdot f$" results significantly greater than the expected maximum flow celerity. For the tests used for the validation presented in this work (see also section 6.1), the studied frame is 455 pixels long (from the crest of the dike to the right end of the frame) that corresponds to a length of approximately s=5.3 cm and the average camera sampling frequency f is set 106 fps. The product $s \cdot f$ is therefore 5.6 m/s. The maximum flow celerity measured in these tests is 1 m/s and significantly lower than $s \cdot f$. This means that no significant flow is escaping from the framing window.

5.2. Steady flow

The procedure might also miss part of the overtopping volumes if pseudo-steady flow conditions occur, determining almost identical overtopping areas and leading therefore to consecutive zero-increments of ΔV. Actually, steady flow hardly occurs in case of wave-induced overtopping. Anyway, it could be addressed by including in the procedure a control on the instantaneous values of the areas of wave overtopping (i.e., of the blue contoured areas of "water" beyond the dike crest in Figure 4a,b for example) to check the presence of consecutive identical values that would be cancelled by the image subtraction. However, this is out of the scope of the present contribution, which deals with experiments on wave overtopping exclusively, and it is just mentioned as a warning for future, different applications.

5.3. Three-dimensional effects

The camera lens determines a slightly perspective distortion of the images, which may generate apparent 3D effects of the overtopping flow. Such effect is visible in the blurred elements presented in the background of the frames of Figure 5, behind the blue-contoured areas. These background elements, characterized by different light and color shades, were not grouped into the "overtopping flow" cluster (cluster 3, with reference to Figure 2a) during the image clustering, but into a different cluster (cluster 4, with reference to Figure 2a), and therefore they are not considered for the calculation of the wave overtopping volumes. In the example of Figure 8, the contours of the clusters 3 and 4 of $frame_6$ are marked with blue and red colors, respectively. In most cases, the elements of the background are correctly grouped into cluster 4. However, it may seldom happen that few of these elements are wrongly grouped into cluster 3 and mistook for foreground elements, leading to a slight overestimation of the total V. The opposite case (i.e. the clustering of foreground elements in cluster 4) was never observed. The quantification of such an overestimation is hard even with the human supervision of the algorithm, because – as pointed out at the beginning of Section 5 – it is difficult to correct establish by eye-examination whether an element belongs to the foreground or to the background. On the contrary, it is extremely more likely that the automatic clustering makes the correct choice, based on quantitative information (pixel values) and not on a 'subjective' analysis of the frame. Therefore, it was decided to accept such a small overestimation and link it to the random uncertainty associated with the whole methodology, avoiding the human intervention that would compromise the automatization of the procedure and would introduce a subjective bias in the computation of the overtopping volumes.

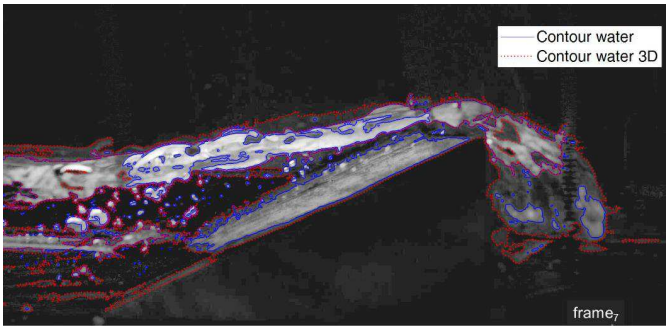

Figure 8. Refined contour (blue) of the cluster "water" detected in one frame and refined contour (red) of the elements present in the background of the image and grouped into a separate cluster.

5.4. Fragmentation of the overtopping tongue

When the overtopping flow overcomes its peak, with the beginning of the decay phase, the overtopping tongue tends to fragment in smaller areas propagating forward and downward chaotically. If the same element of overtopping flow moves into a completely different part of the framing window from one frame to the next one, there is the possibility of counting more than once the same overtopping contribution. This phenomenon was observed for the tests considered in the present contribution and it is evident in the frames from 6 to 12 of Figure 5. As it can be appreciated from this Figure, which shows the result of the image subtraction applied to the same sequence of frames, the procedure is still able to deal with the greater fragmented areas (all the white and green areas do not contribute to the calculation of V, as null or negative increments, respectively), but some smaller areas are likely to be calculated twice. This is the case, for example, of the magenta areas circled in blue (Figure 9a, 8c and 8d). Such areas – which contribute to the calculation of V as positive contribution – do not correspond to real increments of wave overtopping, but they are fragments of the compact overtopping tongue area of the previous frames (Figure 9a).

Note that a fragment present at $frame_i$ and not at $frame_{i-1}$ and at $frame_{i+1}$ would give an overall null contribution to V if the image subtraction operation kept also the negative values. Indeed, if $\Delta V_f>0$ is the volume of a generic fragment present at $frame_i$ resulting from the subtraction of $frame_i – frame_{i-1}$, at the following step $frame_{i+1}$, where the fragment is not present anymore, the subtraction $frame_{i+1} – frame_i$ gives $\Delta V_{f_i}<0$. The sum of the two contributions would be zero. However, the procedure keeps only positive areas (see point iv) of Section 4.1 and the negative contribution $\Delta V_{f_i}<0$ is eliminated, leading to a sum equal to + ΔV_f:

It may also happen that a fragment of flow in the background is temporarily mistaken for a foreground element and therefore wrongly clustered into cluster 3 instead than into cluster 4 (see Sub-section 5.3). If the wrong clustering happens for one frame only, namely at $frame_i$, the image

subtraction counts a positive contribution of that fragment to the total V that should not be accounted.

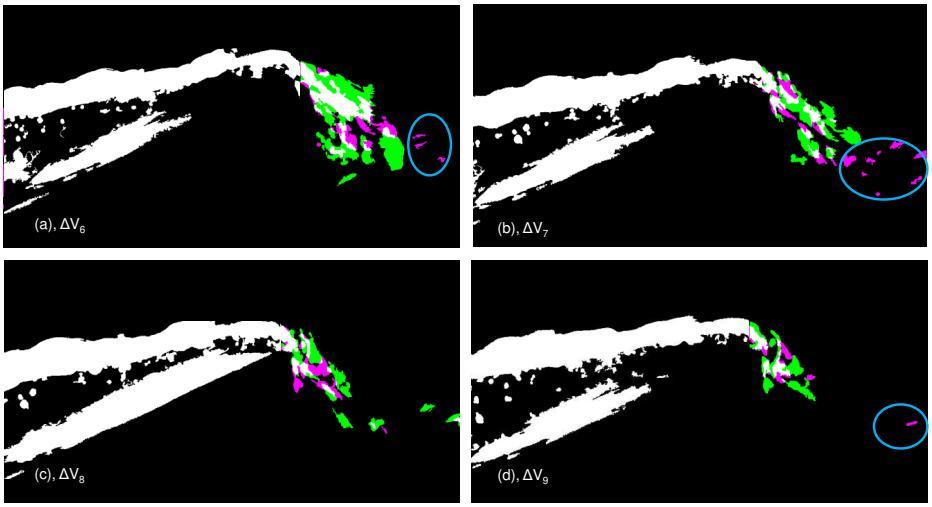

Figure 9. Result of the subtraction of 4 consecutive frames showing the fragmentation of the overtopping tongue occurring at the beginning of the decay phase of the event (magenta: positive, green: negative and white: zero increment of wave overtopping volumes). The blue circles identify areas that are likely to be calculated twice in the calculation of the overtopping procedure.

A specific procedure to remove the "small" fragmented areas was developed to avoid, or at least to reduce, the overestimation of the overtopping volumes. The "small" fragmented areas are identified by their size and by the coordinates of their centroids. All the areas whose size is lower than 500 pixels, i.e. approximately $1 \cdot 10^{-5}$ $m^3/(m \cdot frame)$, and whose centroids are located out of the bounding-box surrounding the main (i.e. biggest) overtopping area, are eliminated. Figure 10, displaying the areas resulting from the image subtraction of the four consecutive frames 6, 7, 8 and 9 and highlights with red rectangles the "small" areas that are eliminated with such procedure. The threshold value of $1 \cdot 10^{-5}$ $(m \cdot frame)$ can be considered as the "0" of the wave overtopping volumes. In other terms, $1 \cdot 10^{-5}$ $(m \cdot frame)$ represents the sensitivity – or the level of accuracy – of the technique here presented and applied. Such value was selected as compromise between accuracy and necessity to limit the overestimation of the volumes caused by the areas fragmentation.

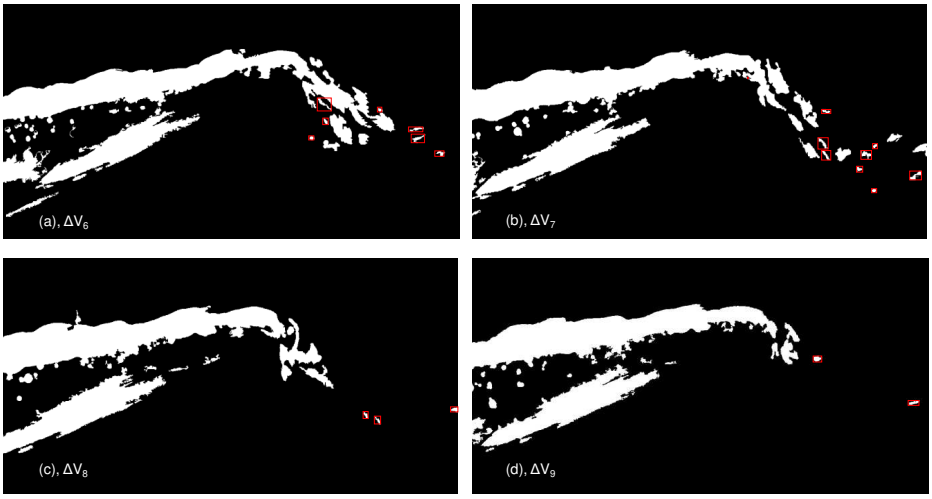

Figure 10. Elimination of the small "fragmented" areas (bounded in red rectangles) contributing to the calculation of the overtopping volumes for 4 consecutive frames.

Overall, it should be noted that the effects related to the "wave escape" and the occurrence of "steady flow" (described in Sub-sections 5.1and 5.2, respectively), which may cause potential underestimations of V, are counterbalanced by the effects of 3D distortion (Sub-section 5.3) and of "area fragmentation" (present Sub-section), that lead to overestimation.

5.5. Variability of the wave overtopping process

Test control and repeatability are critical aspects when considering the accuracy of a single measurement related to wave overtopping. Addressing variability and ensuring test repeatability are interconnected challenges with implications for the reliability and validity of experimental findings. Accurate and consistent measurements are essential for test repeatability. Regular calibration of instruments, such as wave gauges and sensors, mitigates uncertainties related to measurement errors and contributes to the reliability of the experimental data. Slight variations in hydrodynamic conditions, such as the initial still water level, can have a direct impact on test repeatability. Although precise standardized protocols are employed to enhance test repeatability, experience shows that WSI processes, especially those that are quite turbulent, are affected by high variability (Marzeddu et al., 2017; Williams et al., 2019). Therefore, analyzing such processes involves uncertainties inherent to the phenomenon itself, as well as those related to the measurement techniques or algorithms used.

6. Validation and application of the proposed methodology for overtopping volume assessment

This Section presents the results of the methodology for the prediction of the overtopping volumes by means of image clustering applied to the experiments described in Section 2. Sub-section 6.1 compares the results of the image clustering applied to experiment Test_α2m22.6 with the corresponding laboratory measurements. Sub-section 6.2 presents the application of the procedure of image clustering to new experiments, presenting completely different characteristics with respect to experiment Test_α2m22.6 mostly in terms of dike and foreshore layout, and illustrates some potential further applications of the procedure. Sub-section 6.3 finally illustrates the results of the of the procedure of automatic detection of the frames of beginning and ending of the overtopping events.

6.1. Validation versus direct overtopping volume measurements

The image clustering methodology was applied to calculate the overtopping volumes V resulting from 10 repetitions of test Test_α2m22.6, which were named "FWG 1", "FWG 2", …, "FWG 10", as listed in Table 2. The V-values are reported in m^3/m and compared to the corresponding laboratory measurements of the overtopping volumes (4 repetitions). For FWG 1 and FWG 2, the direct comparison is available, and the relative error between the values of V obtained with the image clustering and the corresponding measurements are 13% and 16%, respectively. For all the repetitions, the average overtopping volume estimated with the image clustering technique is μ=1.34 l/m. Instead, the average measured overtopping discharge is 1.25 l/m. Standard deviation is σ=0.23 l/m and σ=0.28 l/m, respectively. Average and standard deviation values are reported in the last two rows of Table 2. The relative errors between the μ-and the σ-values are 9% and - 6%, respectively. The positive signs of the relative errors (+13% and +16% for FWG 1 and FWG 2 and +9% on average) denote that image clustering tends to slight overestimate the measurements.

Table 2. Values of the total overtopping volumes calculated for each repetition of the test Test_α2m22.6 resulting from the image clustering (second column) and measured in the lab channel (third column). The average (μ) and the standard deviation (σ) are reported in the last two rows. The relative errors between estimated and measured V-values are given in the last column, when available.

Test_α2m22.6	estimated with im. cl. V [m^3/m]	measured in channel V [m^3/m]	relative error [-]
FWG 1	$1.17 \cdot 10^{-3}$	$1.04 \cdot 10^{-3}$	0.13
FWG 2	$1.33 \cdot 10^{-3}$	$1.15 \cdot 10^{-3}$	0.16
FWG 3	$1.68 \cdot 10^{-3}$	NaN	
FWG 4	$1.22 \cdot 10^{-3}$	NaN	
FWG 5	$1.59 \cdot 10^{-3}$	NaN	
FWG 6	$1.11 \cdot 10^{-3}$	NaN	

FWG 7	$1.11 \cdot 10^{-3}$	NaN	
FWG 8	$1.69 \cdot 10^{-3}$	NaN	
FWG 9	$1.31 \cdot 10^{-3}$	NaN	
FWG 10	$1.15 \cdot 10^{-3}$	NaN	
FWG 11	NaN	$1.66 \cdot 10^{-3}$	
FWG 12	NaN	$1.13 \cdot 10^{-3}$	
average μ	**$1.34 \cdot 10^{-3}$**	**$1.25 \cdot 10^{-3}$**	**0.09**
standard deviation σ	**$2.33 \cdot 10^{-4}$**	**$2.81 \cdot 10^{-4}$**	**-0.06**

The computation of the ΔV-values from the image clustering does not only provide an estimation of the total overtopping volumes but it also allows a frame-by-frame analysis of the evolution of the instantaneous overtopping discharge. This technique has an advantage over more conventional measurement techniques, where the presence of a chute to collect overtopping flows can make it difficult to detect the instantaneous rate of change of variables, such as the overtopping volume. Figure 11, shows the frame-by-frame values of ΔV for the cases "FWG 1" and "FWG 2" (panels a and b, respectively) of test Test_α2m22.6 and indicates that, for each repetition of the test, two overtopping events were observed, distant approximately 50 frames – viz ≈0.47 s –and lasting between 15 and 18 frames (≈0.14 - 0.17 s) each. The second event determines the maximum instantaneous value of ΔV – which varies between 2.3 and $2.4 \cdot 10^{-4}$ $m^3/(m \cdot frame)$ throughout the 12 repetitions of the test –, whereas the first event determines the larger (60-70%) contribution to the total overtopping volume. Each overtopping event is characterized by a slightly asymmetric wave shape, characterized by a shorter rise phase and a longer decay phase. The asymmetricity is more pronounced in the second overtopping event, where the decay case lasts almost twice the time of the rise phase. Such considerations may result important for practical applications apart from the pure estimation of the overtopping volumes.

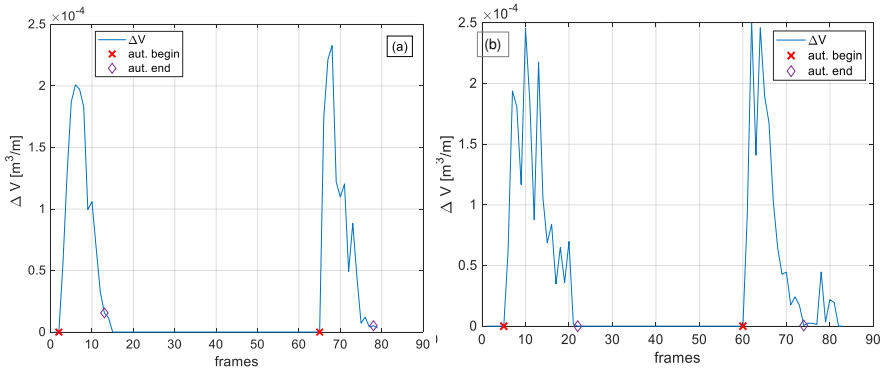

Figure 11. Time evolution of instantaneous increment of wave overtopping volumes ΔV with automatic identification of the beginning and ending of the overtopping events. Application to "FWG 1" (a) and to "FWG 2" (b) of test Test_α2m22.6.

6.2. Applications and potentialities of the methodology

To test the robustness of the procedure developed, three further experiments conducted in non-optimal conditions of lightning and filming, with different geometrical layout and breaking conditions were carried out. These tests are named Test_α1m6.3, Test_α0.5m6.3 and Test_α0.5m22.6_hor, following what described in Section 2. The wave conditions of the first two tests differ from the Test α2m22.6 in terms of focus phase, being equal to 270°.The final test, Test_α0.5m22.6_hor, differs from the validation test Test α2m22.6 as there is a horizontal bottom (i.e. a berm) placed between the landward end of the foreshore slope and the dike toe.

Figure 12 shows the refined contours of the overtopping flow for three frames selected as representative of each of the three tests. For these tests, the differences in the overtopping phenomenon with respect to experiment Test α2m22.6 analyzed in Sub-section 6.1 are huge and evident. The overtopping and the amount of air bubbles entrapped in the water phase is significantly larger and the fragmentation rate is considerable. Nonetheless, the pattern recognition of the overtopping flow highlighted by the blue contours in Figure 12 remains meaningful and enables the computation of the total overtopping volumes, which are reported in Table 3. For each test, this Table provides two values of V, estimated by applying the two functions "regionprops" and "bwarea" of *Matlab ®*: "regionprops" returns the values of the area of each single connected component of the "overtopping flow" cluster, and the ΔV-value of each frame is given by the sum of such areas; "bwarea" directly provides the sum of all the areas of all the connected components composing the "overtopping flow" cluster in a frame, and therefore it directly provides ΔV. As it can be appreciated from the values of Table 3, the differences in the estimations of V obtained with the two methods vary between the 2% and the 11%.

As a final remark, the example case of Test_α1m6.3 (Figure 12a) highlights the importance of properly setting up the camera framing window: in this picture, indeed, the splash of the water is so big that part of it falls beyond the right boundary of the fame. The filming conditions (focus, framing window size, resolution, etc.) should be customized to meet the characteristic of each experiment.

Table 3. Values of the total overtopping volumes calculated for the tests "Test_α2m22.6" (two repetitions, "FWG 1" and "FWG 2"), Test_α1m6.3 and Test_α0.5m6.3 resulting from the image clustering.

	Method of computation	
TEST	regionprops V [m^3/m]	bwarea V [m^3/m]
Test_α2m22.6_hor FWG 1	$2.64 \cdot 10^{-3}$	$2.97 \cdot 10^{-3}$
Test_α2m22.6_hor FWG 2	$5.94 \cdot 10^{-3}$	$6.60 \cdot 10^{-3}$
Test_α1m6.3	$2.40 \cdot 10^{-3}$	$2.46 \cdot 10^{-3}$
Test_α0.5m6.3	$1.02 \cdot 10^{-3}$	$1.05 \cdot 10^{-3}$

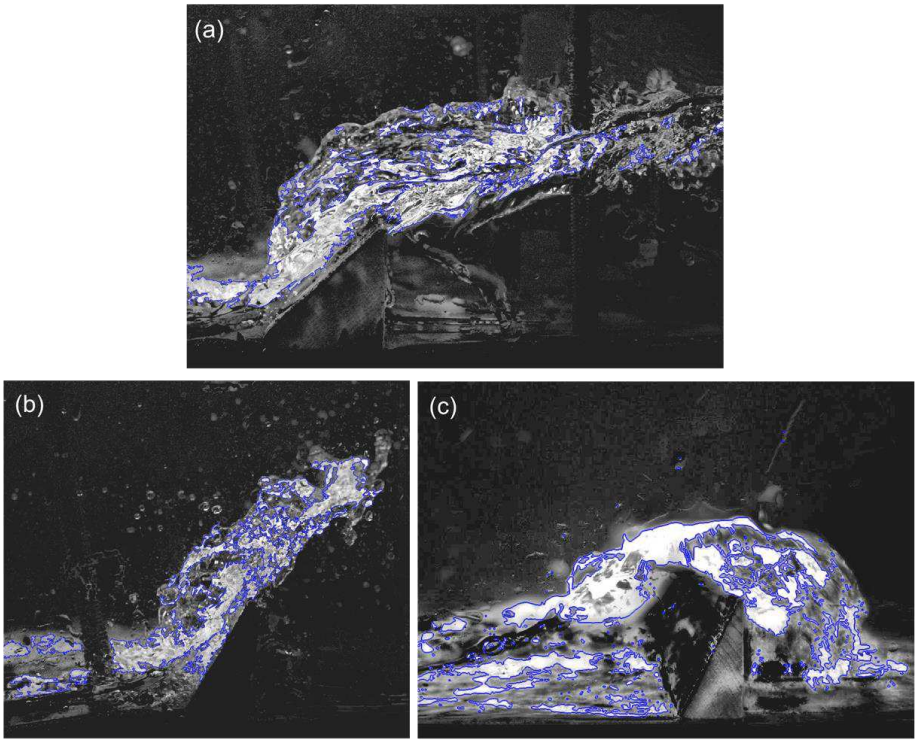

Figure 12. Refined contours (blue) of the cluster "water" detected in three example frames taken from experiments Test_α1m6.3 (a), Test_α0.5m6.3 (b) and Test_α2m22.6_hor (c).

6.3. Results of the automatic individuation of the overtopping events module

This Sub-section discusses the results of the application of the module for the automatization of the detection and separation of the single overtopping events illustrated in Sub-Section 4.2. Such automatic module was applied to all the experiments introduced in the present contribution and the results given in Table 2 and Table 3 actually derive from the automatized procedure.

Figure 11 and Figure 13 show the frame-by-frame evolution of the ΔV-values for the cases "FWG 1" and "FWG 2" of experiment Test_α2m22.6 and for the tests Test_α2m22.6_hor and Test_α1m6.3, respectively – the red crosses and the violet diamonds mark the frames automatically individuated to trigger the beginning and the ending of the computation of the overtopping volumes.

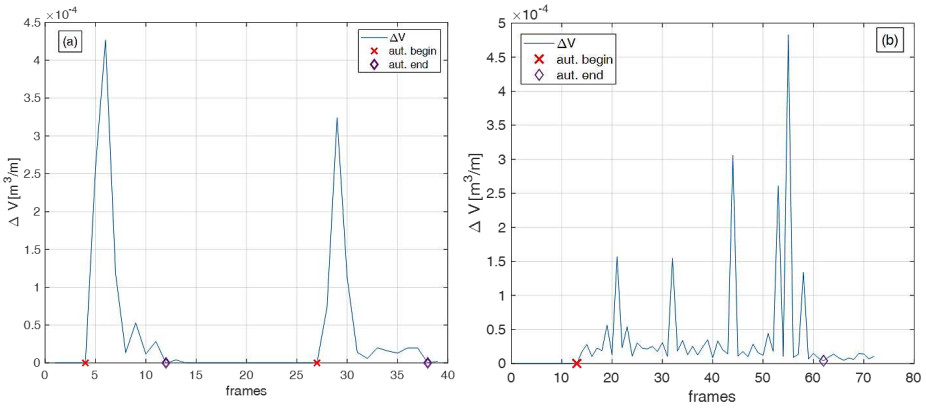

Figure 13. Time evolution of instantaneous increment of wave overtopping volumes ΔV with automatic identification of the beginning and ending of the overtopping events. Application to test Test_α2m22.6_hor (a) and to test Test_α1m6.3 (b).

In Figure 11 and Figure 13a, the distinct overtopping events associated to the same wave are correctly individuated by the automatic module. Such distinct events do correspond to the real overtopping processes observed in the laboratory. An eye-analysis of the frames confirms the duration of each overtopping event – in terms of frames – and the interval between them. For all these tests, the triggering procedure identifies the same beginning and ending frame that a human-driven analysis would have identified.

The test associated to Figure 13b presents a more complex scenario to identify the single overtopping event, but also in this case, the automatic module is capable to select the correct beginning and end of the event at the frames 13 and 62 respectively, though the ΔV-function does not fully drop to 0 at this frame. By eye-analyzing the overtopping process it can be confirmed that also for this case the overtopping starts at frame 13 and continues interruptedly until frames 62-63, when it reduces significantly to drops and sprays that are removed by the procedure as "small" fragmentated areas (see Sub-section 5.4). The contribution of the ΔV-values after frame 62 is lower than 10^{-5} m^3/m, giving a negligible incidence to the total overtopping volume of $2.46 \cdot 10^{-3}$ m^3/m (see Table 3).

7. Discussion and conclusions

This study presents a novel approach using image clustering techniques to analyze wave overtopping volumes on coastal structures. This method allows for a detailed frame-by-frame analysis of wave overtopping flow and discharge, providing insights that traditional measurement techniques may struggle to capture. The experimental model setup in the CIEMito wave flume provided a controlled environment for studying wave overtopping on different dike slopes and

foreshore geometries. This allowed for the development and validation of the image clustering methodology for estimating overtopping volumes. The experiments conducted in the CIEMito were filmed and the image clustering was applied to the video-records to automatically recognize and group different objects in images related to wave overtopping, such as water, air, and solid structures. The setup of proper light conditions represents a key element for the pursuit of good results.

The study also highlights the use of focused wave groups in the experimental setup for assessing wave overtopping on coastal structures. Focused wave groups offer advantages in accurately simulating wave conditions and interactions with structures, complementing traditional irregular wave tests. By incorporating short-duration focused wave groups, researchers can achieve increased repeatability, assess model and scale effects, and improve measurement resolution for large wave interactions. Additionally, focused wave groups eliminate the need for wave absorption and have been validated for WSI problems.

A multi-step procedure for clustering images has been developed for measuring overtopping volumes. The procedure comprises image preprocessing techniques, cluster training, criteria for identifying relevant clusters, and methods for quantifying volumes based on the clustered data. A module was introduced in the procedure to automatically recognize the beginning and the ending of each single overtopping event. Such aspect is fundamental to apply the procedure to train of irregular waves, avoiding the human screening of the video-records. Of course, the filming of irregular wave experiments will require additional data storage capacity and extra elaboration time.

The accuracy and robustness of this non-intrusive overtopping measurement have been assessed by comparing it with direct measurements carried out in the CIEMito flume. A focused wave group was repeated twelve times to measure the overtopping volume over a sloping dike (1V:2H) with a gentle and shallow foreshore (1V:22.6H). The values of standard deviation for both estimations via image clustering and direct measurements are one order of magnitude lower than the single values of the volume and the mean value of all tests. Therefore, the variability of the volumes resulting from image clustering is comparable to that of direct measurements. This variability is likely due to the intrinsic randomness of turbulent phenomena and laboratory effects. The average relative error between volume measurements obtained with the image clustering and the experimental data is 9%.

In addition, the technique was applied to three test cases with varying wave conditions and geometrical layouts. For example, one case had a significantly larger amount of air bubbles entrapped in the water phase and a considerable fragmentation rate. However, the automatic detection and quantification of individual overtopping events appears consistent. It is important to note that a comparison with direct experimental measurements is currently missing and will require further evidence, which could be provided by ad-hoc numerical modelling in future works.

Uncertainties may arise during the application of the methodology. The study notes that effects like insufficient image acquisition speed and pseudo-steady flow conditions may lead to potential underestimations of overtopping volumes. These effects need to be considered alongside

uncertainties related to area fragmentation and 3D distortion, which can cause overestimations. In addition, it is important to consider using automatic overtopping detection instead of relying solely on human oversight. While humans may face challenges in accurately classifying elements within images, automatic clustering based on quantitative pixel values is more likely to make accurate decisions. It is recommended to opt for a slight overestimation rather than human intervention to maintain objectivity and automation in the process.

Finally, the study's findings contribute to the advancement of techniques for assessing coastal structure resilience against wave overtopping events. By combining image clustering with wave overtopping analysis, researchers can gain valuable insights into the dynamics of overtopping flows and their impact on coastal structures.

Authors Declaration Section

Conflict of Interest Statement

The authors have no conflicts to disclose.

Author contributions

Conceptualization, C.A., S.M.F and B.Z.; formal analysis, C.A., S.M.F; investigation, C.A., S.M.F, A.M.; data curation, C.A., S.M.F, A.M.; writing—original draft preparation, C.A., S.M.F. and B.Z.; writing—review and editing, C.A., A.M. and B.Z.; supervision, C.A. and B.Z.

Data availability statement

The data that support the findings of this study are available from the corresponding author upon reasonable request.

Acknowledgments

This work was supported by the project GLORIA PID2020-115030RJ-I00 financed by MCIN/AEI/10.13039/501100011033 "Adquirir conocimientos sobre el riesgo de rebase para las zonas costeras urbanizadas". Besides, Dr. Corrado Altomare acknowledges funding from Spanish government and the European Social Found (ESF) under the programme 'Ramón y Cajal 2020' (RYC2020-030197-I / AEI / 10.13039/501100011033). The support of the European Commission through the Horizon 2020 project BRIGAID ("BRIdging the GAp for Innovations in Disaster resilience," www.brigaid.eu, grant agreement No 700699) is gratefully acknowledged.

References

Adibhusana MN, Lee J-I, Kim Y-T, Ryu Y., 2023. Study of Overtopping Flow Velocity and Overtopping Layer Thickness on Composite Breakwater under Regular Wave. Journal of Marine Science and Engineering 11(4):823. https://doi.org/10.3390/jmse11040823

Adibhusana M.N., Ryu, Y., 2024. Image-Based Measurement Method of Overtopping Flow Velocity and Layer Thickness in Irregular Wave Conditions, Journal of Coastal Research 116(sp1), 41-45, 10.2112/JCR-SI116-009.1

Altomare, C.; Suzuki, T.; Chen, X.; Verwaest, T.; Kortenhaus, A. Wave overtopping of sea dikes with very shallow foreshores. Coast. Eng. 2016, 116, 236–257, doi:10.1016/j.coastaleng.2016.07.002

Altomare, C.; Gironella, X.; Suzuki, T.; Viccione, G.; Saponieri, A. Overtopping Metrics and Coastal Safety: A Case of Study from the Catalan Coast. J. Mar. Sci. Eng. 2020a, 8, 556. https://doi.org/10.3390/jmse8080556

Altomare, C.; Laucelli, D.B.; Mase, H.; Gironella, X. Determination of Semi-Empirical Models for Mean Wave Overtopping Using an Evolutionary Polynomial Paradigm. J. Mar. Sci. Eng. 2020b, 8, 570. https://doi.org/10.3390/jmse8080570

Altomare, C., Gironella, X. and A. J.C.Crespo, 2021. Simulation of random wave overtopping by a WCSPH model, Applied Ocean Research, Vol. 116, 102888. https://doi.org/10.1016/j.apor.2021.102888

Blenkinsopp, C.E.; Baldock, T.E.; Bayle, P.M.; Foss, O.; Almeida, L.P.; Schimmels, S., 2022. Remote Sensing of Wave Overtopping on Dynamic Coastal Structures. Remote Sens. 2022, 14, 513. https://doi.org/10.3390/ rs14030513

Buscombe, D., Carini, R.J., Harrison, S.R., Chickadel, C.C., Warrick, J.A., 2020. Optical wave gauging using deep neural networks. Coastal Engineering 155, 103593. http://dx.doi.org/10.1016/j.coastaleng.2019.103593.

Canny, J., 1986. A computational approach to edge detection. IEEE Trans. Pattern Anal. Mach. Intell, 8, 679–714.

Cao D., Chen H., Yuan J., 2021. Inline force on human body due to non-impulsive wave overtopping at a vertical seawall, Ocean Engineering 219, 108300, https://doi.org/10.1016/j.oceaneng.2020.108300.

Chen, W., Warmink, J.J., van Gent M.R.A., Hulscher, S.J.M.H., 2021. Numerical modelling of wave overtopping at dikes using OpenFOAM®, Coastal Engineering 166, 103890, https://doi.org/10.1016/j.coastaleng.2021.103890.

Chi, Sh., Zhang, C., Sui, Tt. et al., 2021. Field observation of wave overtopping at sea dike using shore-based video images. J Hydrodyn 33, 657–672. https://doi.org/10.1007/s42241-021-0073-1.

Crespo A.J.C., Domínguez J.M., Rogers B.D., Gómez-Gesteira M., Longshawb S., Canelas R., Vacondio R., Barreiroa A. and García-Feal O., 2015. DualSPHysics: Open-source parallel CFD solver based on Smoothed Particle Hydrodynamics (SPH), Computer Physics Communications 187, 204-216. https://doi.org/10.1016/j.cpc.2014.10.004

Deane, G., Stokes, M. 2002. Scale dependence of bubble creation mechanisms in breaking waves. Nature 418, 839–844. https://doi.org/10.1038/nature00967

Dempster, A. P., Laird, N. M. and Rubin, D. B., 1977. Maximum likelihood from incomplete data via the EM algorithm. Journal of the Royal Statistical Society. Series B (Methodological), 39(1), 1–38.

Den Bieman, J. P., de Ridder, M. P., and van Gent, M. R. A., 2020. Deep learning video analysis as measurement technique in physical models, Coastal Eng. 158, 103689. https://doi.org/10.1016/j.coastaleng.2020.103689

Den Bieman J.P., van Gent M.R.A., van den Boogaard H.F.P, 2021. Wave overtopping predictions using an advanced machine learning technique. Coastal Engineering 166, 103830. https://doi.org/10.1016/j.coastaleng.2020.103830

Domínguez, J.M., Fourtakas, G., Altomare; C., Canelas, R.B., Tafuni, A., García-Feal, O., Martínez-Estévez, I., Mokos, A., Vacondio, R., Crespo, A.J.C., Rogers, B.D., Stansby, P.K., Gómez-Gesteira. M. 2022. DualSPHysics: from fluid dynamics to multiphysics problems. Computational Particle Mechanics, 9(5), 867-895. doi:10.1007/s40571-021-00404-2.

Duin, R.P.W.; Pekalska, E., 2015. Pattern Recognition: Introduction and Terminology; Delft University of Technology: Delft, The Netherlands. Available online: http://resolver.tudelft.nl/uuid:f5c560ed-5fc7-4320-84b4-a20614012bc7 (last accessed July 1, 2021).

EurOtop, 2018. Manual on wave overtopping of sea defences and related structures. An overtopping manual largely based on european research, but for worldwide application. N.W.H. Allsop, T. Bruce, J. DeRouck, A. Kortenhaus, T. Pullen, H. Schuttrumpf, P. Troch, J.W. van der Meer and B. Zanuttigh. www.overtoppingmanual.com.

Fairley, I., M.A. Davidson, Kingston, K., 2007. Video monitoring of overtopping of detached breakwaters in a mesotidal environment. Proc. 5th Coastal Structures International Conf., 1923-1932. 10.1142/9789814282024_0170

Formentin S.M. and Zanuttigh B., 2019. Semi-automatic detection of the overtopping waves and reconstruction of the overtopping flow characteristics at coastal structures, Coastal Engineering 152, 103533, 18 pp.

948 Formentin S.M., Gaeta M.G., Palma G, Zanuttigh B., and Guerrero M., 2019. Flow Depths and
949 Velocities across a Smooth Dike Crest, Water 2019, 11, 2197; doi:10.3390/w11102197.

950 Formentin, S.M.; Gaeta, M.G.; De Vecchis, R.; Guerrero, M.; Zanuttigh, B., 2021. Image-
951 clustering analysis of the wave-structure interaction processes under breaking and non-breaking
952 waves. Physics of Fluids, 33, 105121.

953 Formentin, S.M.; Zanuttigh, B. Statistical Analysis of the Wave Runup at Walls in a Changing
954 Climate by Means of Image Clustering. Water 2023, 15, 2729. https://doi.org/10.3390/
955 w15152729

956 Gallach-Sánchez, D., Troch, P., Kortenhaus, A. 2021. A new average wave overtopping
957 prediction formula with improved accuracy for smooth steep low-crested structures, Coastal
958 Engineering, Volume 163,https://doi.org/10.1016/j.coastaleng.2020.103800.

959 Heller, V. Scale effects in physical hydraulic engineering models. J. Hydraul. Res. 2011, 49,
960 293–306.

961 Hofland B., Diamantidou E., van Steeg P., Meys P., 2015. Wave runup and wave overtopping
962 measurements using a laser scanner. Coastal Engineering 106, 20–29.

963 Hughes, S.A., Thornton, C.I., 2016. Estimation of time-varying discharge and cumulative volume
964 in individual overtopping waves. Coast Eng. 117, 191–204.

965 Ingram D., Bruce T., Allsop W., 2008. Post-overtopping loads behind vertical structures,
966 Proceedings of the 31st International Conference, Hamburg, Germany, 2008, pp.3144-3156.
967 https://doi.org/10.1142/9789814277426_0260

968 Jacobsen, N.G., Fuhrman, D.R., Fredsøe, J., 2012. A wave generation toolbox for the open-
969 source CFD library: OpenFoam®. Int. J. Numer. Methods Fluid., 70 (9) (2012), pp. 1073-1088,
970 10.1002/fld.2726

971 Koosheh, A., Etemad-Shahidi, A., Cartwright, N., Tomlinson, R., van Gent, M.R.A. 2022
972 Distribution of individual wave overtopping volumes at rubble mound seawalls, Coastal
973 Engineering, Volume 177, https://doi.org/10.1016/j.coastaleng.2022.104173.

974 Koosheh, A., Etemad-Shahidi, A., Cartwright, N., Tomlinson, R., van Gent, M.R.A. 2024. Wave
975 overtopping layer thickness on the crest of rubble mound seawalls, Coastal Engineering, Volume
976 188, https://doi.org/10.1016/j.coastaleng.2023.104441.

977 Lashley, C. H., Van Der Meer, J., Bricker, J. D., Altomare, C., Suzuki, T., & Hirayama, K., 2021.
978 Formulating wave overtopping at vertical and sloping structures with shallow foreshores using
979 deep-water wave characteristics. Journal of waterway, port, coastal, and ocean engineering,
980 147(6), 04021036.

981 Mares-Nasarre, P., Argente, G., Gómez-Martín, M.E., Medina, J.R., 2019. Overtopping layer
982 thickness and overtopping flow velocity on mound breakwaters, Coastal Engineering, Volume
983 154, https://doi.org/10.1016/j.coastaleng.2019.103561.

Mares-Nasarre, P., van Gent, M.R.A., Morales-Nápoles, O. 2024. A copula-based model to describe the uncertainty of overtopping variables on mound breakwaters, Coastal Engineering, Volume 189, https://doi.org/10.1016/j.coastaleng.2024.104483.

Marzeddu, A. Oliveira, T.C.A., Gironella, F.X., Sánchez-Arcilla, A. 2017. Variability of wave impact measurements on vertical breakwaters, Journal of Hydraulic Research, 55:6, 772-786, DOI: 10.1080/00221686.2017.1312576

Miller, R.L., 1972. The role of surface tension in breaking waves. Proc. of the 13th Coastal Engineering Conference, Vol. 1. American Society of Civil Engineers, pp. 433–449

Nørgaard, J.Q.H., Lykke Andersen, T., Burcharth, H.F., 2014. Distribution of individual wave overtopping volumes in shallow water wave conditions. Coast Eng. 83, 15–23.

Oosterlo, P., Hofland, B., Van der Meer, J., Overduin, M., Steendam, G. J., 2021. Field measurements of very oblique wave run-up and overtopping with laser scanners. Journal of Coastal and Hydraulic Structures, 1. https://doi.org/10.48438/jchs.2021.0006

Pearson, J., Bruce, T., Allsop, N. W. H. & Gironella, X. 2002. Violent wave overtopping – measurements at large and small scale. Proc. ICCE, ASCE, pp 2227–2238

Raby A., Jayaratne R., Bredmose H. and Bullock G., 2020. Individual violent wave-overtopping events: Behaviour and estimation. J. Hydraul. Res. 58, 34-46.

Ray S.D., 2002. Applied Photographic Optics (Oxford: Focal), Routledge, pp 215–233.

Peter K. Stansby, Tong Feng, 2004. Surf zone wave overtopping a trapezoidal structure: 1-D modelling and PIV comparison, Coastal Engineering 51(5–6), 483-500. https://doi.org/10.1016/j.coastaleng.2004.06.001.

Raby, A., Jayaratne,R., Bredmose, H., Bullock, G., 2020. Individual violent wave-overtopping events: behaviour and estimation, Journal of Hydraulic Research, 58:1, 34-46, DOI: 10.1080/00221686.2018.1555549

Schüttrumpf, H., Oumeraci, H., 2005. Layer thicknesses and velocities of wave overtopping flow at seadikes. Coast. Eng, 52, 473–495

Stagonas, D., Warbrick, D., Muller, G., Magagna, D. 2011. Surface tension effects on energy dissipation by small scale, experimental breaking waves. Coastal Engineering, 58 (9), 826-836. doi:10.1016/j.coastaleng.2011.05.009.

Stringari, C.E., Harris, D.L., Power, H.E., 2019. A novel machine learning algorithm for tracking remotely sensed waves in the surf zone. Coastal Engineering 147, 149–158. http://dx.doi.org/10.1016/j.coastaleng.2019.02.002.

Stringari, C.E., Veras Guimarães P., Filipot J.F, Leckler F., Duarte R., 2021. Deep neural networks for active wave breaking classification, Scientific Reports 11:3604. https://doi.org/10.1038/s41598-021-83188-y

1019 Suzuki, T.; Altomare, C.; Yasuda, T.; Verwaest, T. Characterization of Overtopping Waves on
1020 Sea Dikes with Gentle and Shallow Foreshores. J. Mar. Sci. Eng. 2020, 8, 752.
1021 https://doi.org/10.3390/jmse8100752

1022 van Gent, M.R.; Wolters, G.; Capel, A., 2022. Wave overtopping discharges at rubble mound
1023 breakwaters including effects of a crest wall and a berm. Coast. Eng. 176, 104151.

1024 Violeau, D., 2012. Fluid Mechanics and the SPH Method: theory and Applications, Fluid
1025 Mechanics and the SPH Method: theory and Applications.
1026 https://doi.org/10.1093/acprof:oso/9780199655526.001.0001.

1027 Whittaker, C.N., Fitzgerald, C.J., Raby, A.C., Taylor, P.H., Borthwick, A.G.L., 2018. Extreme
1028 coastal responses using focused wave groups: Overtopping and horizontal forces exerted on an
1029 inclined seawall, Coastal Engineering 140, 292-305,
1030 https://doi.org/10.1016/j.coastaleng.2018.08.004.

1031 Williams, H.E.; Briganti, R.; Romano, A.; Dodd, N., 2019. Experimental Analysis of Wave
1032 Overtopping: A New Small Scale Laboratory Dataset for the Assessment of Uncertainty for
1033 Smooth Sloped and Vertical Coastal Structures. J. Mar. Sci. Eng. 7, 217.
1034 https://doi.org/10.3390/jmse7070217

1035 Yuhi, M., Mase, H., Kim, S., Umeda, S., Altomare, C. 2021. Refinement of integrated formula of
1036 wave overtopping and runup modeling, Ocean Eng., 220:108350.
1037 https://doi.org/10.1016/j.oceaneng.2020.108350.

1038 Zanuttigh, B., van der Meer, J.W., Bruce, T., Hughes, S., 2013. Statistical characterisation of
1039 extreme overtopping wave volumes. In: Proc ICE, Coasts, Marine Structures and Breakwaters
1040 2013, Edinburgh, UK.

1041 Zanuttigh, B., Formentin, S.M., Van der Meer, J.W., 2016. Prediction of extreme and tolerable
1042 wave overtopping discharges through an advanced neural network. Ocean Eng. 127, 7–22.

1043